Supplementary Information

Flexoelectricity-driven giant polarization in (Bi, Na)TiO_3-based ferroelectric thin films

Yunlong Sun[1], Ranming Niu[2,3], Zizheng Song[4,5], Shiyu Tang[6], Huizhong Wang[1], Xun Geng[7], Ji Zhang[1,8], Jack Yang[1,8], Claudio Cazorla[9], Changqing Guo[6], Shery L. Y. Chang[1], Xiaojie Lou[10], Houbing Huang[6,*], Zibin Chen[4,5,*], Shujun Zhang[11] and Danyang Wang[1,*]

[1] School of Materials Science and Engineering, The University of New South Wales, Sydney, NSW 2052, Australia

[2] Australian Centre for Microscopy and Microanalysis, The University of Sydney, Sydney, NSW 2006, Australia

[3] School of Aerospace, Mechanical and Mechatronic Engineering, The University of Sydney, Sydney, NSW 2006, Australia

[4] State Key Laboratory of Ultra-Precision Machining Technology, Department of Industrial and Systems Engineering, The Hong Kong Polytechnic University, Kowloon, Hong Kong, China

[5] Research Institute for Advanced Manufacturing, Department of Industrial and Systems Engineering, The Hong Kong Polytechnic University, Hong Kong, China

[6] Advanced Research Institute of Multidisciplinary Science, Beijing Institute of Technology, Beijing 100081, China.

[7] Global Innovative Center for Advanced Nanomaterials, College of Engineering, Science and Environment, The University of Newcastle, Callaghan, New South Wales, 2308, Australia

[8] Materials and Manufacturing Futures Institute, The University of New South Wales, Sydney, NSW 2052, Australia

[9] Departament de Física, Universitat Politècnica de Catalunya, Campus Nord B4-B5, E-08034 Barcelona, Spain

[10] Frontier Institute of Science and Technology, State Key Laboratory for Mechanical Behavior of Materials and Future Industrial Innovation Institute of Emerging Information Storage and Smart Sensor, Xi'an Jiaotong University, Xi'an, 710049, China

[11] Department of Chemistry, City University of Hong Kong, Hong Kong, China

* Corresponding author

hbhuang@bit.edu.cn, zi-bin.chen@polyu.edu.hk, and dy.wang@unsw.edu.au

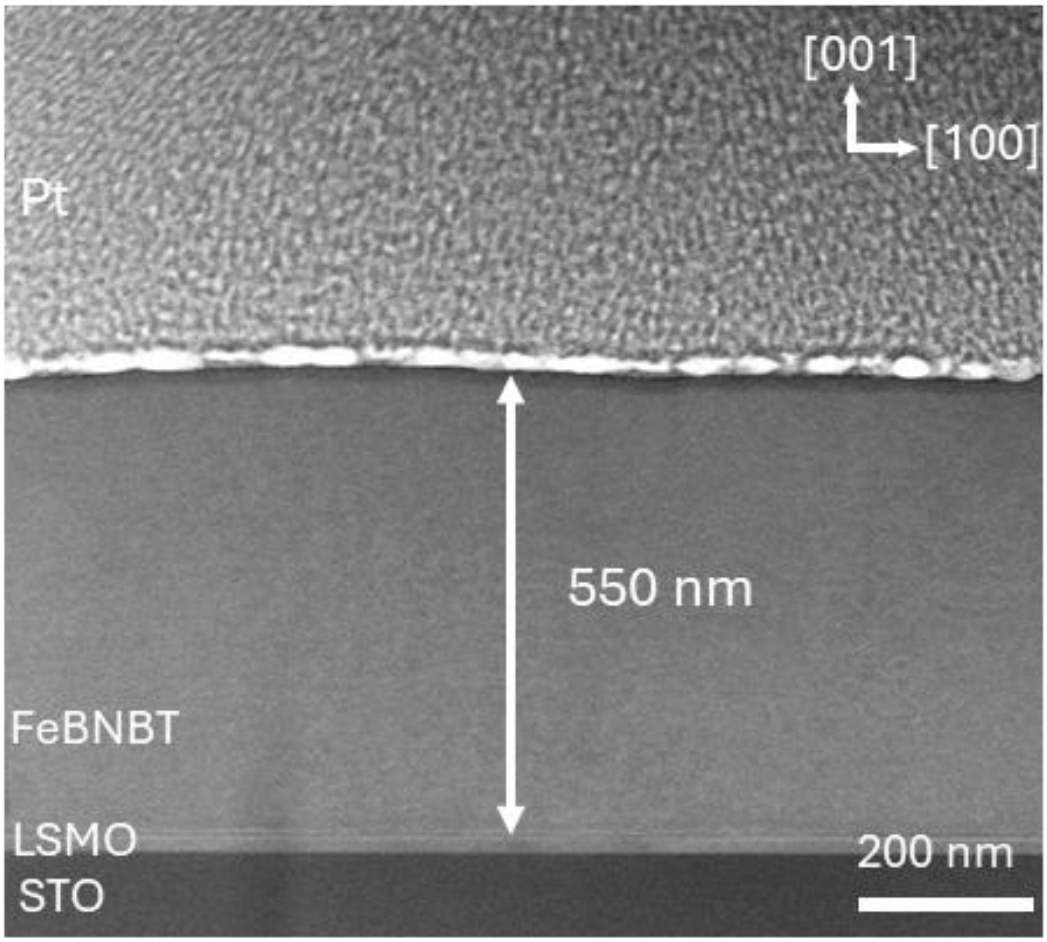

Supplementary Figure 1. Low-magnification HAADF-STEM image of Fe-BNBT thin films.

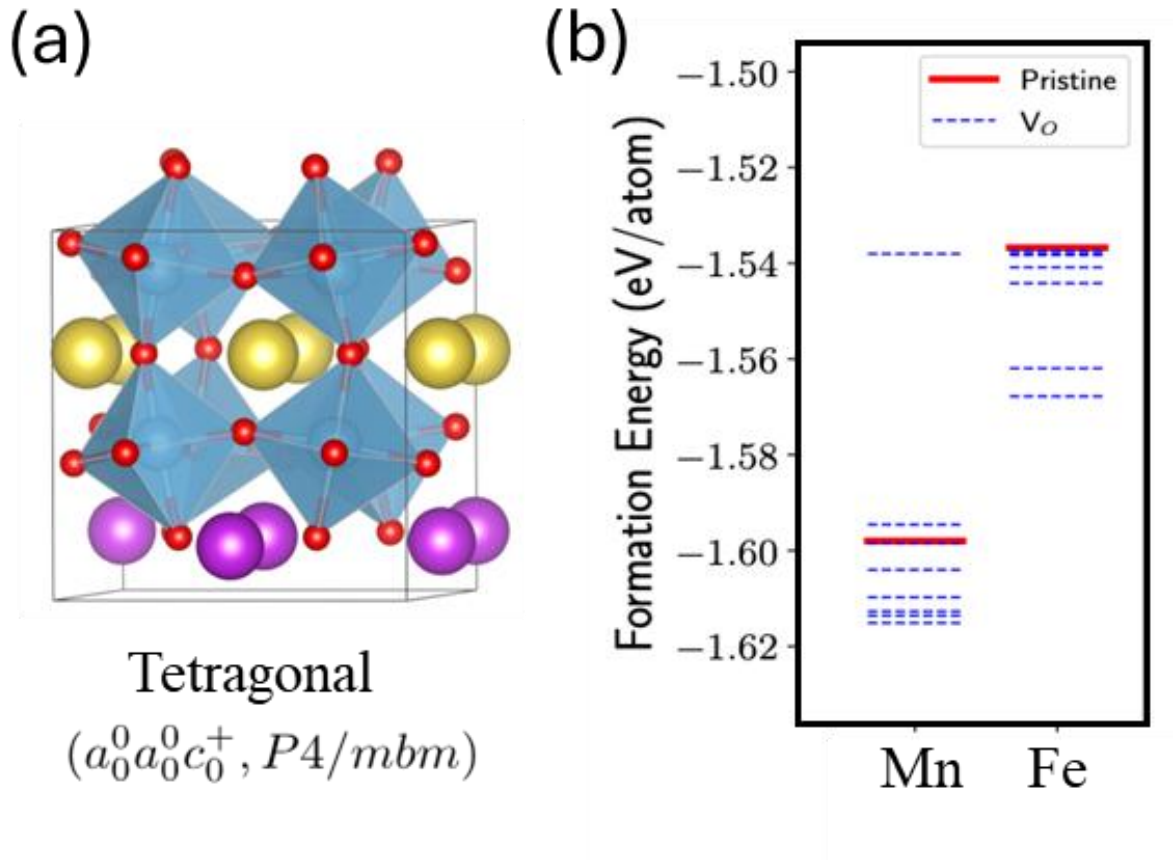

Supplementary Figure 2. (a) The schematic diagram of the tetragonal unit cell of BNBT for the DFT calculation, where purple, yellow, and red spheres represent Bi, Na, and O atoms, respectively. (b) The formation energy of Mn-doped and Fe-doped BNBT unit cells with oxygen vacancy-related defects and without oxygen vacancy-related defects. The solid red lines depict the formation energy of BNBT unit cells without any oxygen vacancy-related defects while the blue dashed lines represent the formation energy of BNBT unit cells with oxygen vacancy occurring in various positions in the lattice structures. The lower the formation energy, the more stable the BNBT structures. [1]

The emergence of H-H and T-T domain walls is intrinsically linked to the alignment of oxygen vacancies along specific crystallographic directions. [2-4] While the domain walls can reorient in response to an external electric field, the ordered distribution of oxygen vacancies, which manifest as planar defects, remains largely unaltered. This stability arises from the elevated activation energy barriers for the migration of oxygen vacancy, particularly in the immediate proximity of dislocations, compared to those in the bulk lattice. [5] As a result, the local strain gradients and the associated flexoelectric effects are preserved under the applied electric fields.

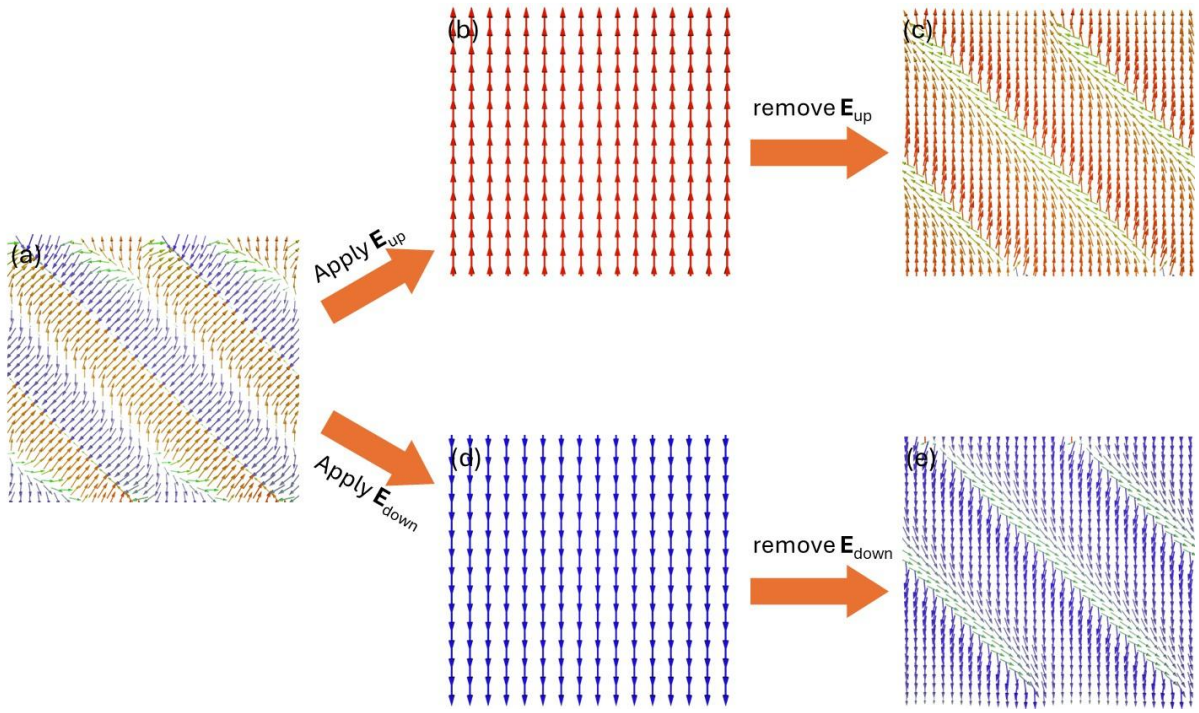

Supplementary Figure 3. (a) Phase field-simulation results depicting the polarization distribution of bound charge-modified Fe-BNBT in various states: (a) initial configuration, (b) under the application of an upward-directed electric field ($\mathbf{E}_{up}$), (c) following the removal of the upward electric field, (d) under the application of a downward-directed electric field ($\mathbf{E}_{down}$), and (e) following the removal of the downward electric field.

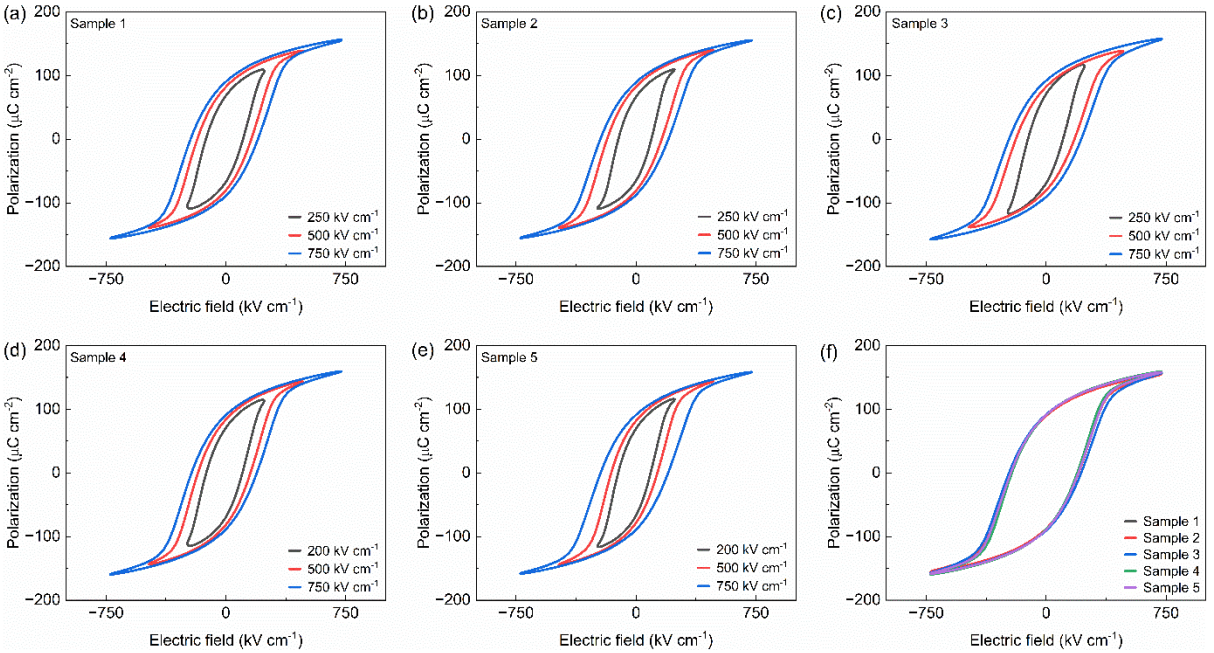

Supplementary Figure 4. (a)-(e)Room-temperature *P*–*E* loops obtained from five Fe-BNBT thin films prepared under optimal processing conditions. (f) Comparison of the *P*–*E* loops of five Fe-BNBT thin films under 750 kV cm^{-1}.

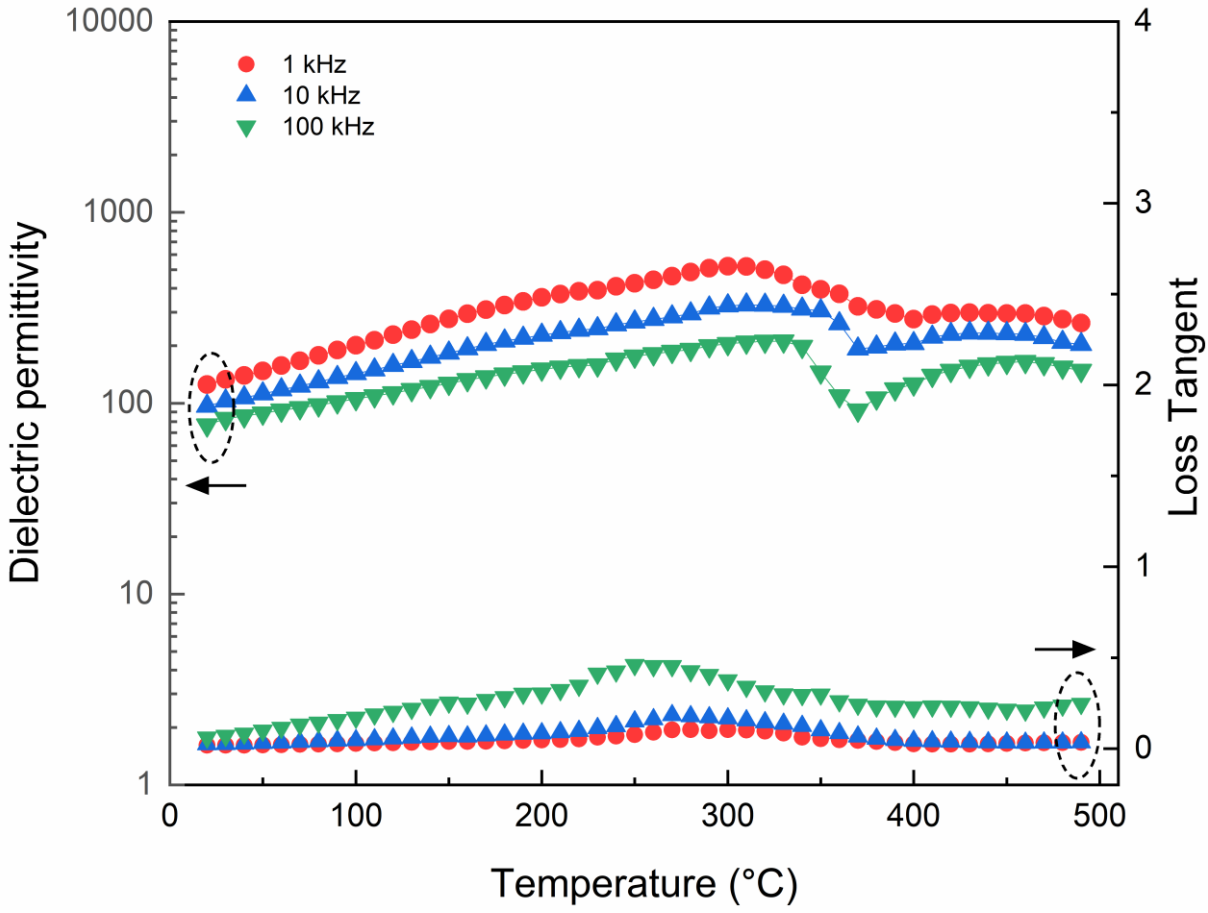

Supplementary Figure 5. Temperature-dependent dielectric properties of Fe-BNBT thin films.

We assessed the relaxor properties of our thin films by calculating the relaxor diffuseness factor, γ, using the modified Curie-Weiss law[6]:

$$\frac{1}{\varepsilon_r} - \frac{1}{\varepsilon_{r,m}} = \frac{(T - T_m)^\gamma}{C}$$

where ε_r is dielectric permittivity at the temperature T, $\varepsilon_{r,m}$ the maximum dielectric permittivity at the temperature T_m, and C the Curie constant. In typical ferroelectrics, γ is expected to be 1, while $\gamma = 2$ suggests an ideal relaxor ferroelectric. Our calculation yielded a γ value of 1.013, as shown in Supplementary Figure 6, which unambiguously suggests a typical ferroelectric behaviour of our Fe-BNBT thin films, rather than a relaxor at a composition close to MPB.

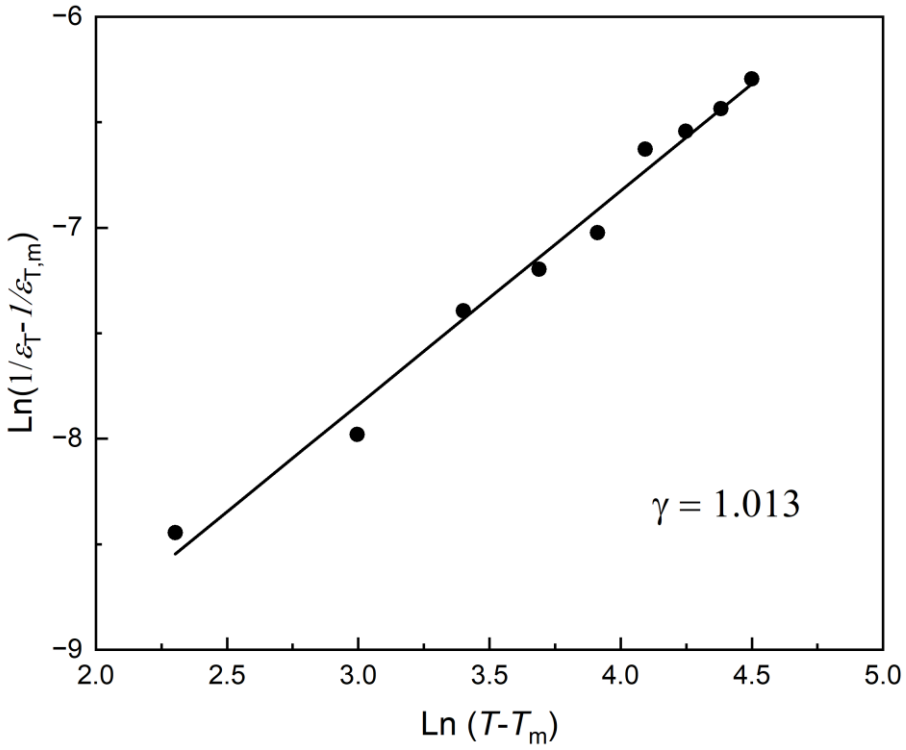

Supplementary Figure 6. Fitting of the relaxor diffuseness factor of Fe-BNBT films based on the temperature-dependent dielectric data.

The leakage current density vs electric field curves at various temperatures of our Fe-BNBT thin films were shown in Supplementary Figure 7. The leakage current density remains as low as ~10^{-4} A cm^{-2} even at elevated temperatures, which is considered minimal for typical ferroelectric thin films possessing a perovskite structure. [7-9] The relatively low leakage current density can be attributed to the trapping of oxygen vacancies and free charges at T-T and H-H domain walls, respectively. These domain walls act as potential barriers that impede charge transport, thereby suppressing the formation and growth of electrical trees and effectively reducing leakage currents, particularly at high temperatures. [10]

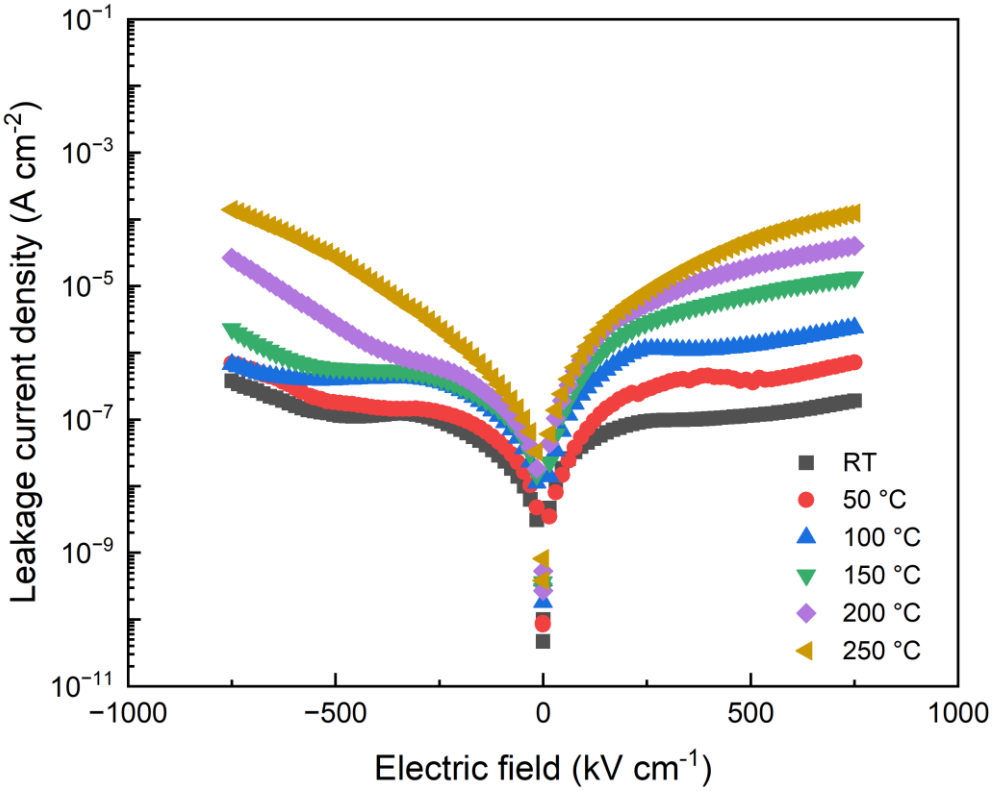

Supplementary Figure 7. Leakage current density as a function of the applied electric fields of Fe-BNBT thin films at various temperatures.

In dielectric thin films, the charge transport is often dominated by bulk-limited conduction mechanisms, including ohmic conduction, space-charge-limited conduction (SCLC), and Poole-Frenkel emission (PF), or interface-limited Schottky emission (SE). [11] The

space-charge-limited current obeys quadratic electric field dependence in the case of discrete traps, [12]

$$J_{SCLC} = 9\mu\varepsilon_0\varepsilon_r E^2/8d$$

where μ is the carrier mobility and d the film thickness. The current density across a Schottky barrier is[12]

$$J_S = A^* T^2 \exp - [(\phi_b - \beta_s E^{\frac{1}{2}})/kT]$$

where $\beta_s = (q^3/4\pi\varepsilon_0\varepsilon_r)^{1/2}$, A^* is the Richardson constant, T the temperature, q the electron charge, ϕ_b the Schottky barrier height, k the Boltzmann constant, ε_0 the permittivity of free space, and ε_r the dielectric constant of the thin film. The Pool-Frenkel conductivity is given by[12]

$$J_{PF} = \sigma_0 E \exp - [(E_1 - \beta_{PF} E^{\frac{1}{2}})/kT]$$

where $\beta_{PF} = (q^3/\pi\varepsilon_0\varepsilon_r)^{1/2}$, σ_0 is a sample-dependent zero-field conductivity, and $\mathbf{E}_1$ is the trap ionization energy. The functional relationship of SE and PF is similar, so that the plots of $\ln(J\ T^{-2})$ versus $\mathbf{E}^{0.5}$ and $\ln(J\ V^{-1})$ versus $\mathbf{E}^{0.5}$ for SE and PF, respectively, will yield linear relationships.

We plotted and fitted the leakage current data based on the above-mentioned transport mechanisms, as shown in Supplementary Figure 8. At room temperature, the leakage current is governed by PF under the electric field < 150 kV cm^{-1}, given the relative dielectric constant extracted from the slope of the linear fits to PF is 118.8, which lies within the physically reasonable range between the optical dielectric constant (6.71) [13] and quasi-static dielectric constant (500- 800) [14] typical for BNT-based thin films.

Apart from the low field region (< 150 kV cm^{-1}), the Schottky emission mechanism becomes dominant, supported by the extracted dielectric constant of 52.8, which is also physically plausible. SCLC can be ruled out in the entire range of measuring temperature and electric field, given slope of the Ln*J*-Ln*E* curves evidently deviates from 2, as shown in

Supplementary Figure 9(a). At 250 °C, the leakage current follows the PF mechanism across the entire range of the measuring electric field.

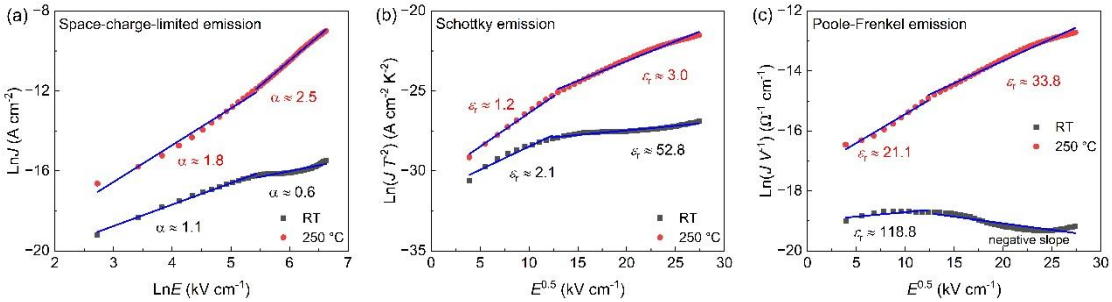

Supplementary Figure 8. Analysis of leakage current mechanisms in Fe-BNBT thin films based on (a) SCLC, (b) SE, and (c) PF emissions.

Although the bright streaks observed in the STEM images exhibit a one-dimensional contrast, i.e., linear features in the projection, the associated planar defects extend beyond these streaks into the adjacent lattice, spanning over approximately 5 unit cells. This broader spatial distribution is confirmed by the line profiles of oxygen atom signal intensities taken from the eight contiguous regions, delineated by blue to green dashed rectangles, as shown in Supplementary Figure 9.

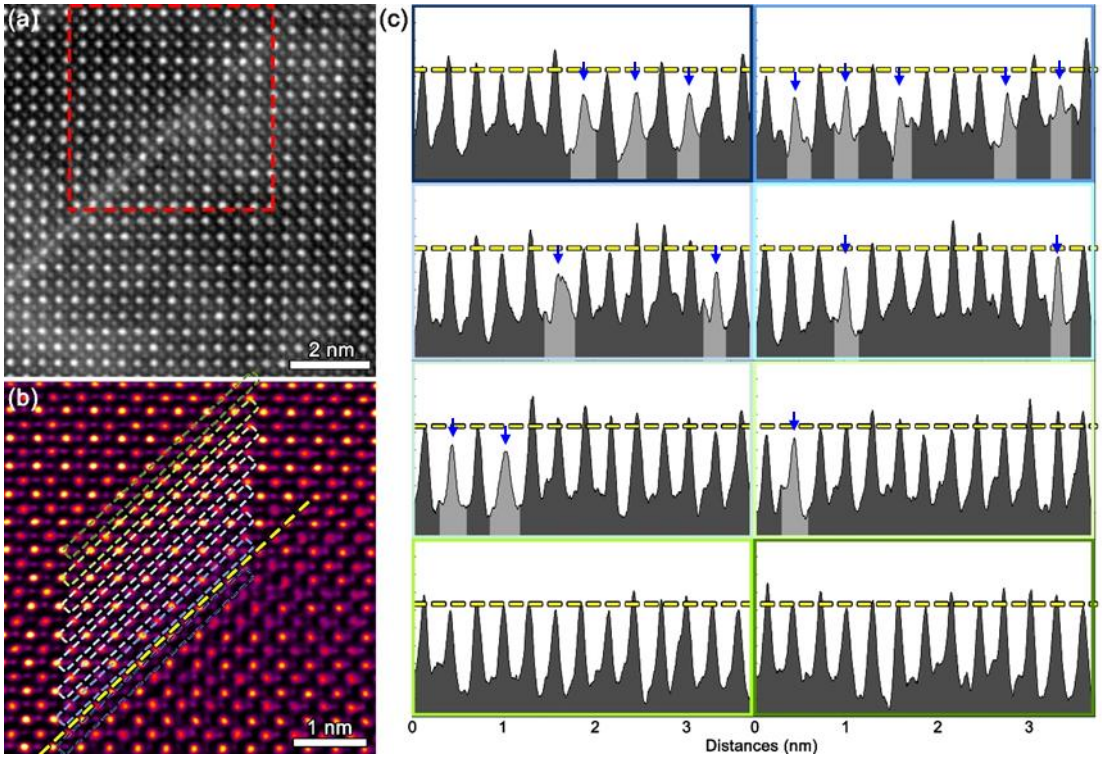

Supplementary Figure 9. (a) HAADF-STEM image of Fe-BNBT thin films. (b) STEM-iDPC image of the region outlined by the red dashed square in (a). The yellow dashed line indicates the position of the bright streak, while the series of colored dashed rectangles represent eight contiguous regions extending outward from the bright streak. (c) Line profiles of oxygen atom signal intensities extracted from the regions marked by the blue to green dashed rectangles in (b), illustrating a progressive decrease in oxygen vacancy concentration from the bright streak toward the surrounding lattice. The blue arrows mark the positions associated with oxygen vacancies.

Based on this analysis, the volume fraction of oxygen vacancy-associated planar defects can be estimated from the STEM images (Supplementary Figure 10) using the line intercept

method, which is a common approach to evaluate the dislocation density in alloys. [15,16] The volume fraction V_{defect} is calculated using the following equation:

$$V_{defect} = \frac{A_{defect}}{A_{film}} = \frac{L_{streak} \times A_{unit\ cell} \times 8 \times \sin 45°}{A_{film}}$$

where A_{defect} and A_{film} represent the total projected area of the planar defects and the cross-sectional area of the thin film, respectively. L_{streak} denotes the cumulative length of the bright streaks, and $A_{unit\ cell}$ corresponds to the projected area of a single Fe-BNBT unit cell. The volume fraction of the planar defects in the Fe-BNBT thin films is estimated to be ~16%.

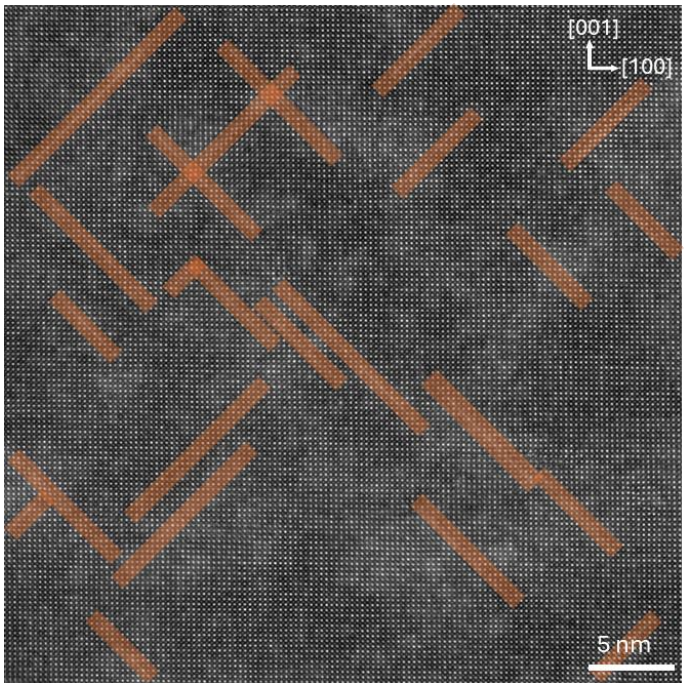

Supplementary Figure 10. HAADF STEM images of Fe-BNBT thin films, with orange-shaded regions indicating the presence of planar defects.

To further investigate the effect of substrate on the polarization of the resulting films, we fabricated 550-nm-thick 2 mol% Fe-doped and Mn-doped BNBT thin films on LSMO-electroded $(LaAlO_3)_{0.3}(Sr_2AlTaO_6)_{0.7}$ (LSAT) (001) single crystal substrates (cubic, a = 3.868 Å) using PLD under the identical deposition conditions to those grown on STO substrates. As shown in Supplementary Figure 11(a) and (b), although the ferroelectric polarizations of both Fe-doped and Mn-doped BNBT films grown on LSAT are slightly lower compared to their counterparts grown on STO, the Fe-BNBT film still exhibits a notably high $\mathbf{P}_m$ of 145 μC cm^{-2} and a $\mathbf{P}_r$ of 96.7 μC cm^{-2}. These values remain substantially higher than those of the Mn-BNBT films on LSAT ($\mathbf{P}_m$ = 49.1 μC cm^{-2}, $\mathbf{P}_r$ = 19.4 μC cm^{-2}). These results suggest that the large polarization of our Fe-BNBT thin films is not strongly dependent on the substrates.

2 mol% Fe-doped BNBT thin films were also directly deposited on Nb-doped STO (Nb:STO) (001) single crystal substrates. As shown in Supplementary Figure 11(c), the considerably large polarizations ($\mathbf{P}_m$ = 110 μC cm^{-2} and $\mathbf{P}_r$ =157 μC cm^{-2}) are highly comparable to those of samples grown on LSMO-electroded STO (001) substrates, strongly underpinning the presence of the oxygen-deficient structures.

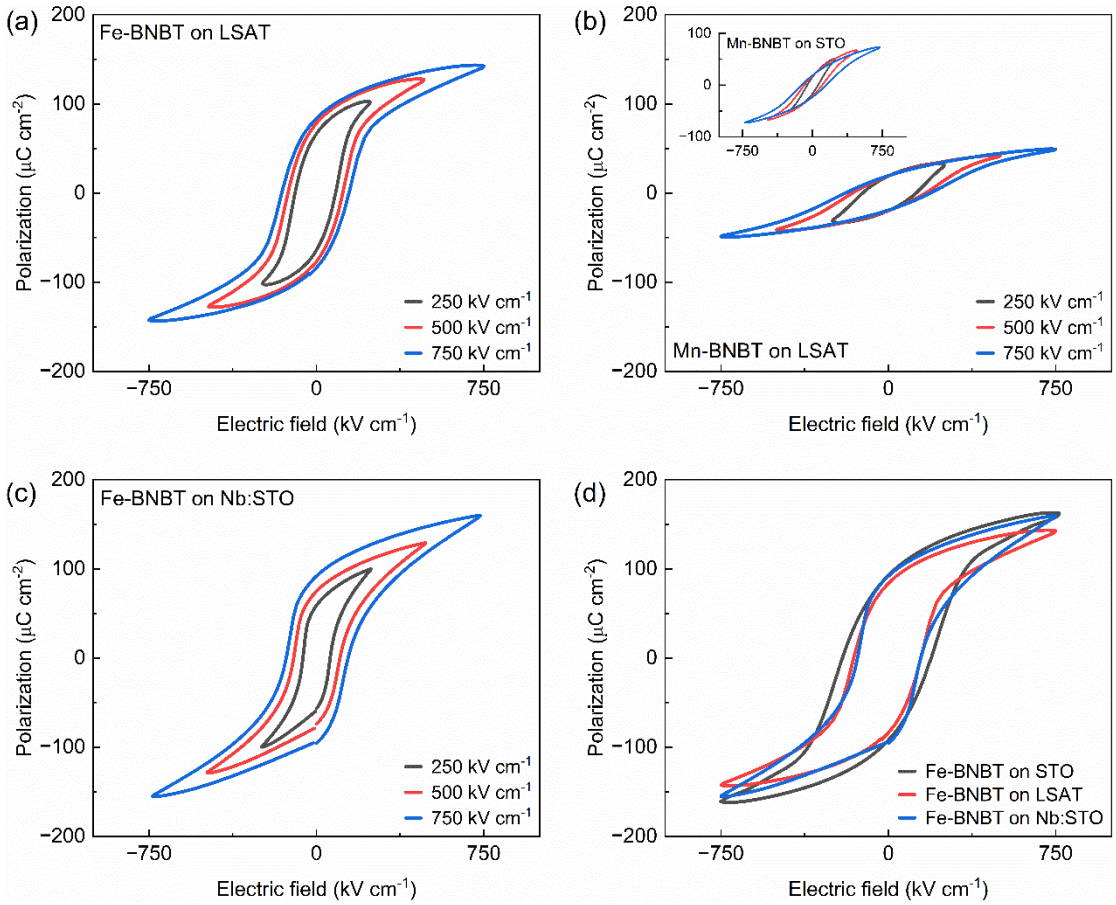

Supplementary Figure 11. Room-temperature *P*–*E* loops of (a) Fe-BNBT thin films and (b) Mn-BNBT thin films deposited on LSAT (001) single crystal substrates, and (c) Fe-BNBT thin films deposited on Nb:STO (001) substrates. The inset in (b) is the *P*-*E* loops of Mn-BNBT deposited on STO (001) substrate. (d) Comparison of the *P*–*E* loops of Fe-BNBT thin films deposited on different substrates.

To understand the effect of Fe doping level on the ferroelectric properties of BNBT-based thin films, we fabricated a series of thin films (350-nm-thick for a quicker screening of doping level) with various Fe contents, i.e., 0.5, 1.0, 1.5, 2.0, 2.5, and 3.0 mol% by PLD. As shown in Supplementary Figure 12, both the maximum and remanent polarization are optimal when the Fe doping level is 2 mol%.

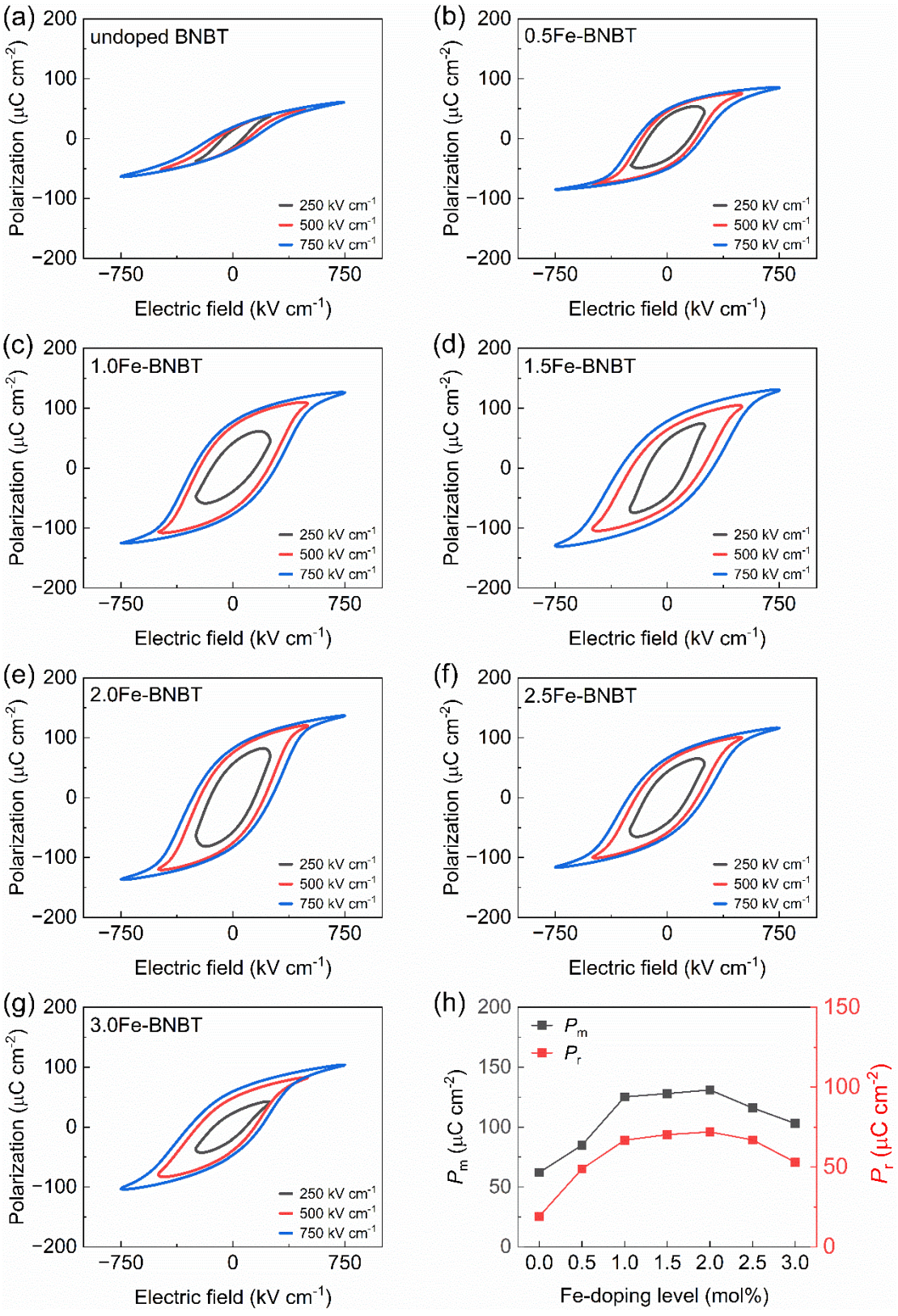

Supplementary Figure 12. Room-temperature *P*–*E* loops of 350 nm-thick BNBT thin films with (a) 0, (b) 0.5, (c) 1.0, (d) 1.5, (e) 2.0, (f) 2.5, and (g) 3.0 mol% Fe doping levels measured under selected electric fields. (h) Evolution of maximum and remanent polarizations of the 350 nm-thick BNBT thin films as a function of Fe doping level.

X-ray photoelectron spectroscopy (XPS) was employed to estimate the level of oxygen vacancy in Fe-BNBT thin films, as shown in Supplementary Figure 13. The relative level of oxygen defects ($O_V\%$) in the sample could be estimated by the:

$$O_V\% = \frac{A_{O_V}}{A_{O_L} + A_{O_V} + A_{O_C}}$$

where A_{O_L}, A_{O_V} and A_{O_C} are the areas enclosed under O_L, O_V, and O_C peak, respectively. The XPS results reveal a progressive increase in oxygen vacancy concentration with the increase in Fe doping level. Nevertheless, an excessive amount of oxygen vacancy (in 2.5 and 3.0 mol% Fe doped samples) will deteriorate the ferroelectric properties, as shown in Supplementary Figure 13, owing to the more pronounced domain-wall pinning effect[17] and increased leakage current[18].

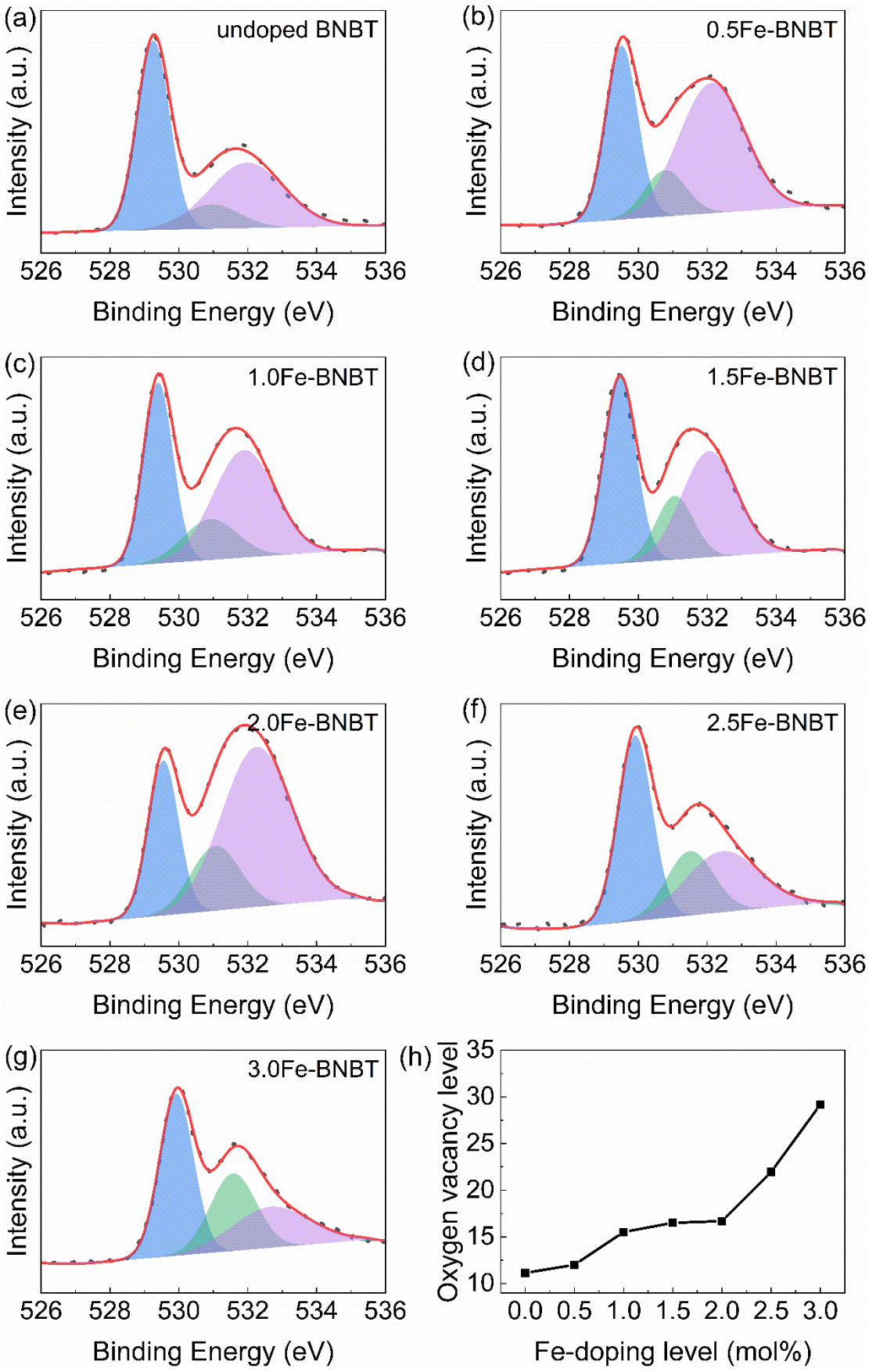

Supplementary Figure 13. XPS spectra of the O 1*s* electronic level for Fe-BNBT thin films with (a) undoped and (b) 0.5, (c) 1.0, (d) 1.5, (e) 2.0, (f) 2.5, and (g) 3.0 mol% Fe doping levels. Blue (O_L), green

(O_V), and purple (O_C) peak is ascribed to the lattice oxygen, lattice oxygen connected with the lower valence cation after vacancy creation, and the adsorbed surface water and/or hydroxyl molecules, respectively. (h) Evolution of the O_V level in BNBT-based thin films as a function of Fe doping level.

The undoped BNBT thin films exhibited a maximum polarization of 62.1 cm^{-2}, whereas 2.0 mol% Fe-doped films showed a significantly enhanced $\mathbf{P}_m$ of 161 μC cm^{-2}. HAADF STEM images confirm the absence of planar defects in the undoped film, as shown in Supplementary Figure 14, suggesting that the oxygen-deficient structures originate from the introduction of Fe dopants and the critical role of the oxygen-deficient structures in boosting the polarization.

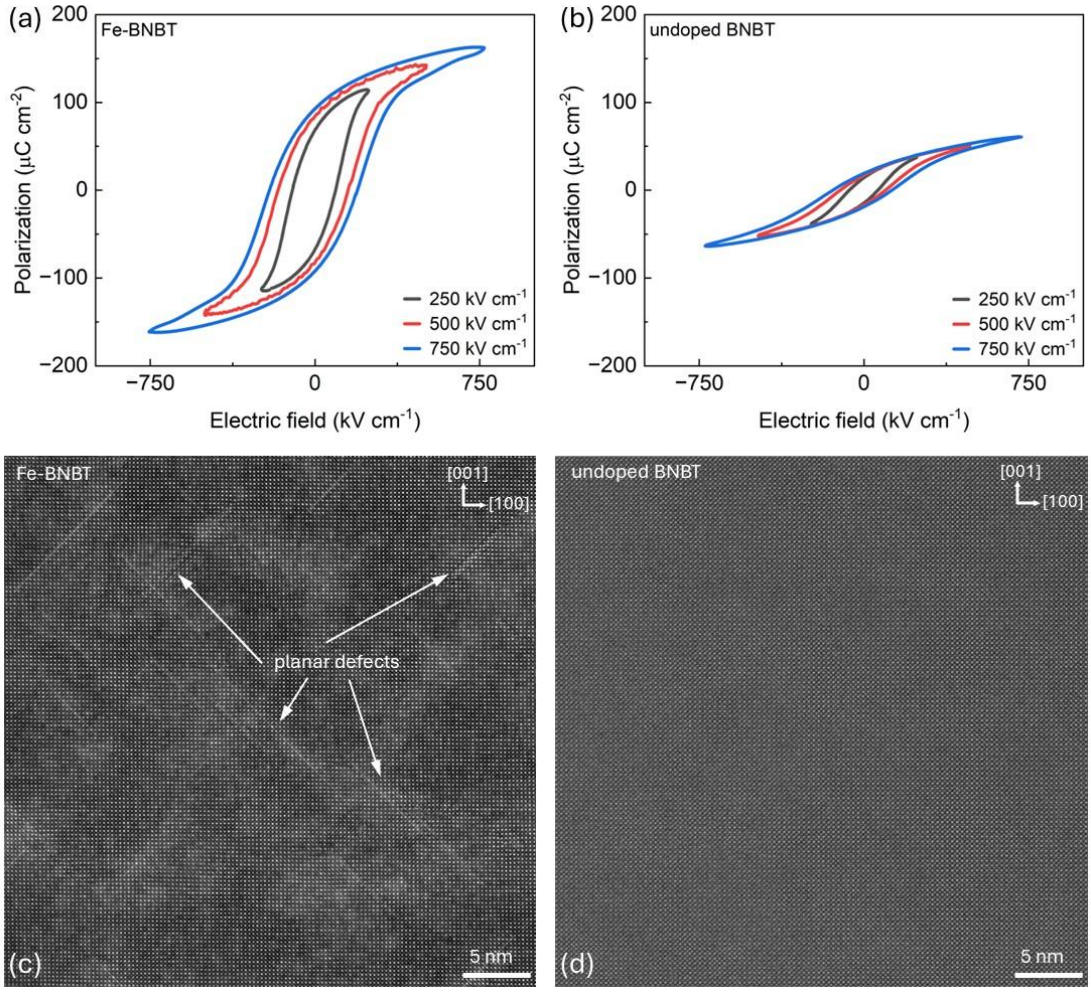

Supplementary Figure 14. Room-temperature *P–E* loops of (a) 2.0 mol% Fe-doped BNBT thin films and (b) undoped BNBT thin films. HAADF STEM images of (c) 2.0 mol% Fe-doped BNBT thin films and (d) undoped BNBT thin films.

These results unequivocally suggest that Fe doping plays a decisive role in enhancing the polarization of BNBT-based thin films. We attribute the giant polarization of Fe-doped BNBT thin films to several fundamental mechanisms as follows:

1) Fe^{3+} (r_{Fe3+} = 58.5 pm) preferentially replaces Ti^{4+} (r_{Ti4+} = 60.5 pm) at the B-site of the perovskite lattice, as an acceptor, leading to the formation of oxygen vacancies to compensate for the charge imbalance. These vacancies tend to organize along specific crystallographic planes, [2,3] as detailed in the response to Comment (4). In contrast, other commonly employed dopants in BNBT lattice such as La^{3+} (r_{La3+} = 136 pm), Sm^{3+} (r_{Sm3+} = 124 pm), and Eu^{3+} (r_{Eu3+} = 129 pm) substitute for A-site cations (r_{Na+} = 139 pm, r_{Bi3+} = 120 pm, r_{Ba2+} = 135 pm) as donors, due to their similar ionic radii to that of the A-site cations, which do not promote the formation of oxygen vacancies. [19]

2) The multivalent nature of Mn (Mn^{2+}, Mn^{3+}, Mn^{4+}) in principle allows them to enter different lattice sites of BNBT. Considering the similarity of the ionic radii between Mn cations (r_{Mn2+} ~ 0.83 Å, r_{Mn3+} ~ 0.65 Å, r_{Mn4+} ~ 0.53 Å) and the respective cations in the host lattice, as well as the global instable index indices calculated in our previous work[20,21], Mn^{2+} prefers to reside in the A-site, and Mn^{3+} and Mn^{4+} are inclined to substitute Ti^{4+} at the B-site. It should be noted that the presence of Mn^{2+} often impedes the formation of oxygen vacancies. [22] More importantly, Mn dopants tend to introduce localized point defects rather than extended planar faults. [23]

3) Co^{3+} (r_{Co3+} = 55 pm) can also substitute for Ti^{4+} at the B-site and is reported to be more effective than Fe in promoting the creation of oxygen vacancies. [24] However, this increased oxygen vacancy concentration is often accompanied by an increased electrical conductivity, which may incur leakage current pathways and deteriorate ferroelectric performance, as shown in Supplementary Figure 15.

To confirm the unique role of Fe doping in enhancing the polarization, 550 nm-thick BNBT thin films doped with 2.0 mol% of a few other commonly adopted dopants in perovskite ferroelectrics, including Mn, La, Sm, Eu, and Co, as well as undoped BNBT thin films were grown on LSMO-electroded STO (001) single crystal substrates using PLD under the same deposition conditions as that for Fe-doped counterparts. Room-temperature *P*-*E* loops of these BNBT-based thin films are presented in Supplementary Figure 15.

The maximum polarization $\mathbf{P}_m$ of undoped, Mn-, La-, Sm-, Eu-, and Co-doped BNBT thin films are 62, 73, 68, 73, 74, and 97 μC cm^{-2}, respectively. In contrast, Fe-doped BNBT thin films exhibit a drastically higher $\mathbf{P}_m$ of 161 μC cm^{-2}.

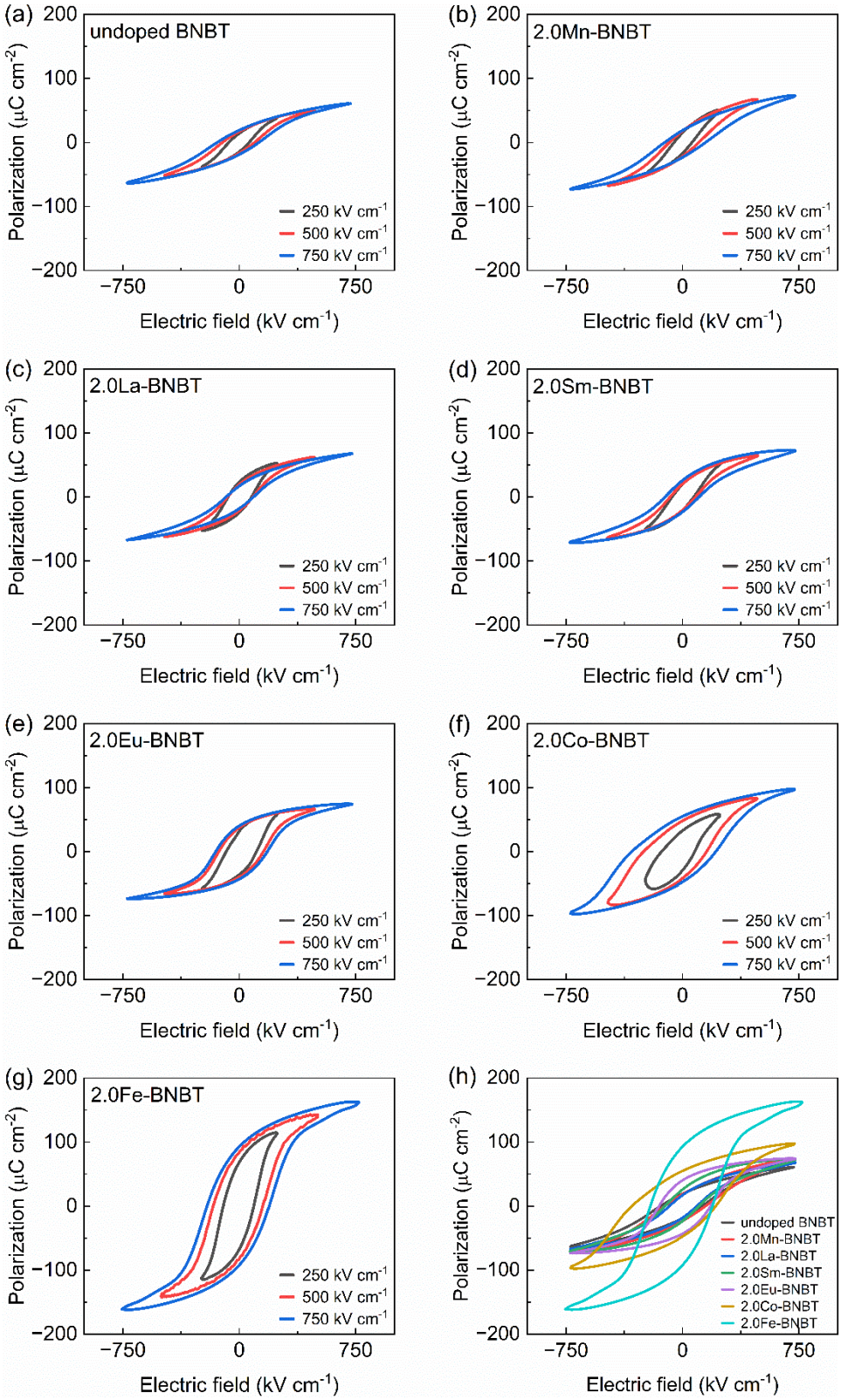

Supplementary Figure 15. Room-temperature *P–E* loops of (a) undoped BNBT thin film and BNBT-based thin films doped with 2.0 mol% of (b) Mn, (c) La, (d) Sm, (e) Eu, (f) Co, and (g) Fe, respectively. (h) Comparison of *P–E* loops of BNBT thin films with different dopants.

To understand the influence of film thickness on the flexoelectric effect and polarization behavior, 2.0 mol% Fe-doped BNBT thin films with thicknesses of 150, 350, 750, and 950 nm were also deposited on STO (001) single crystal substrates by PLD under the same conditions as that for the 550-nm-thick sample. As shown in Supplementary Figure 16, all the Fe-doped BNBT thin films exhibit well-defined *P-E* loops at room temperature with very large polarization (both $\mathbf{P}_m$ and $\mathbf{P}_r$), implying that the flexoelectric effect acts on all the thicknesses.

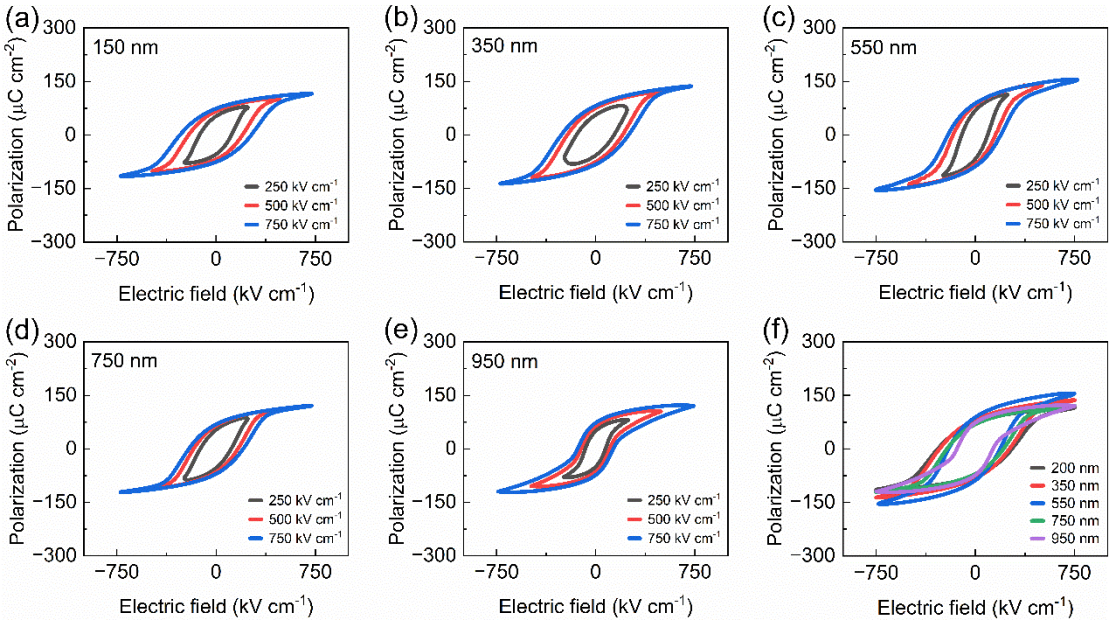

Supplementary Figure 16. The room-temperature *P–E* loops of Fe-BNBT thin films with a thickness of (a) 150 nm, (b) 350 nm, (c) 550 nm, (d) 750 nm, and (e) 950 nm. (f) Comparison of *P–E* loops of Fe-BNBT thin films having different thicknesses.

Multi-dimensional characterizations, including XRD, RSM, and STEM were conducted to perceive the structural origin of the thickness dependence of the observed polarization. The XRD patterns confirm the preferred (*00l*) orientation of all the thin films. Notably, the observation of a broad diffraction peak near 41° on the XRD pattern of the 950 nm-thick Fe-BNBT films suggests the presence of super-tetragonal phase, characterized by a significant *c*-axis expansion, as confirmed in our previous study[25]. RSM scans around the (103) plane of thinner films (150, 350, and 550 nm) indicate that the Q_x values of STO, LSMO, and Fe-BNBT

diffraction spots are almost identical, signifying that LSMO and Fe-BNBT layers remain fully strained on the STO substrate (in-plane direction). However, in the thicker films, i.e., 750 and 950 nm-thick, the Fe-BNBT diffraction spots broaden, suggesting a partial strain relaxation as film thickness increases.

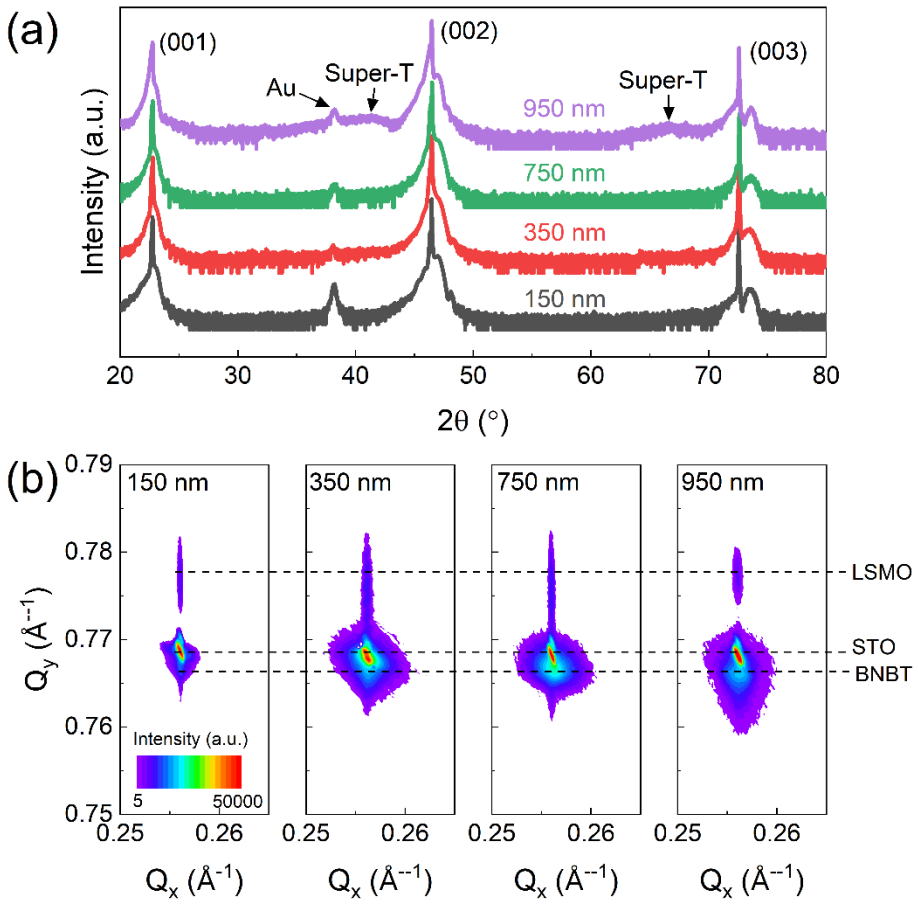

Supplementary Figure 17. (a) XRD θ-2θ scan results of Fe-BNBT thin films having different thicknesses. (b) XRD-RSM around (103) reflections of Fe-BNBT thin films having different thicknesses. Notably, a small bump around 41° is perceived in 950 nm-thick FeBNBT thin films, suggesting the creation of a super-T structure. The appearance of super-T structures may be attributed to the film being too thick, preventing the evaporation of Bismuth from the films during the film growth process.

Low-magnification STEM images of Fe-BNBT thin films with thicknesses of 150, 550, and 950 nm, as shown in Supplementary Figure 18 (a), (b), and (c), respectively, show the difference in the spatial distribution of the defects. We give a closer examination of three representative regions along the thickness of the thin films, i.e. Area 1, near the substrate; Area

2, in the middle of the film; and Area 3, close to the film surface, as marked by the red boxes in Supplementary Figure 18 (a)-(c).

It is evident that the spatial distribution of planar defects is considerably different in the films of different thicknesses:

1) In the 150 nm-thick film, planar defects are barely seen in Areas 1 and 2, but appear sparsely in Area 3.

2) In the 550 nm-thick film, planar defects remain absent in Area 1 but are loosely present in Area 2, with a noticeable increase in density in Area 3.

3) In the 950 nm-thick film, planar defects are still absent in Area 1, while they render a high density in Area 2. However, these defects are barely seen in Area 3, where β-Bi_2O_3 layers begin to develop[25].

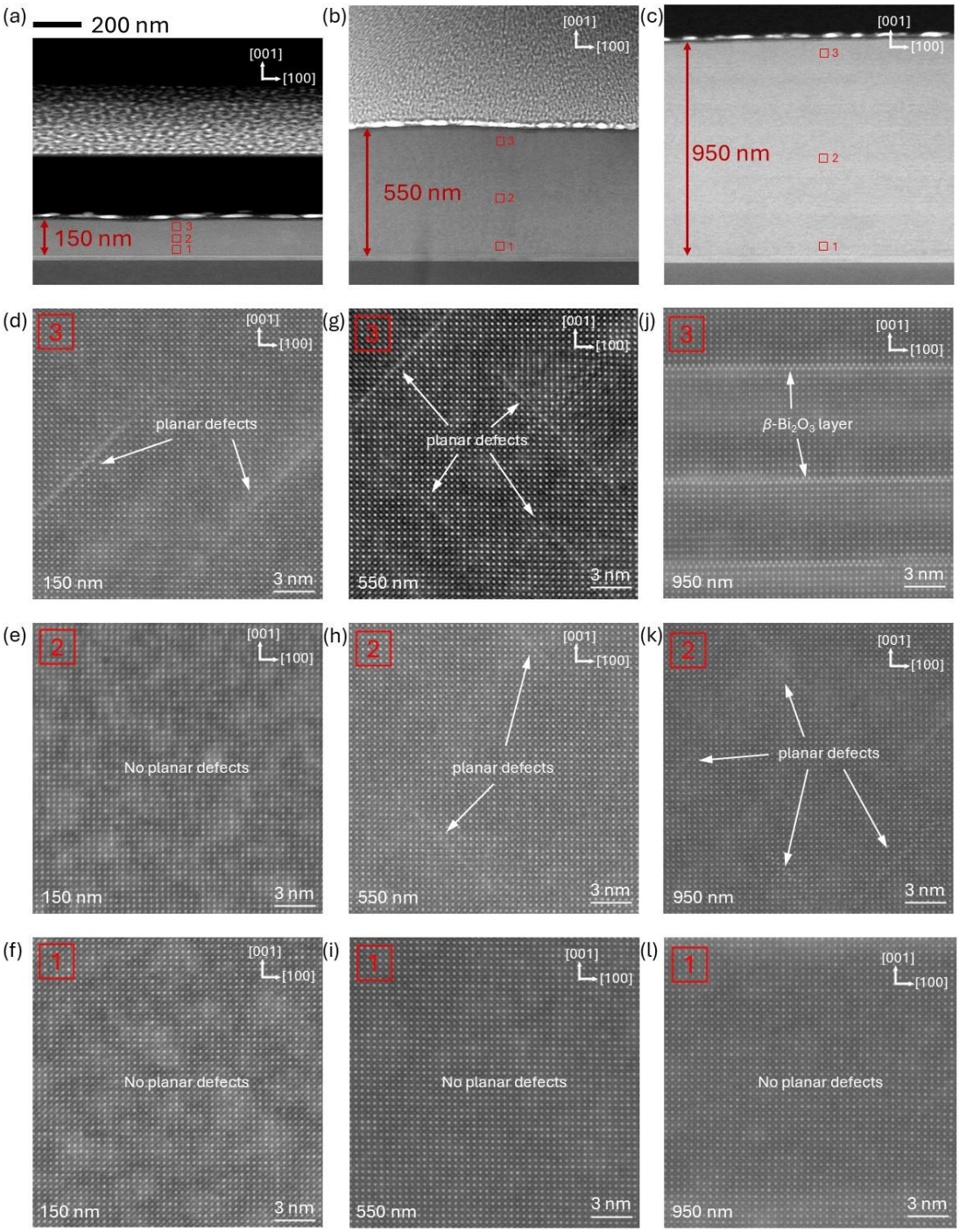

Supplementary Figure 18. Low-magnification HAADF-STEM images of Fe-BNBT thin films with thicknesses of (a) 150 nm, (b) 550 nm, and (c) 950 nm. (d–f) HAADF-STEM images of the 150 nm-thick Fe-BNBT thin film, acquired from Areas 3, 2, and 1, respectively. (g–i) HAADF-STEM images of the 550 nm-thick Fe-BNBT thin film, captured from the corresponding Areas 3, 2, and 1. (j–l) HAADF-STEM images of the 950 nm-thick Fe-BNBT thin film, obtained from Areas 3, 2, and 1, respectively.

It is known that epitaxial thin films with lattice mismatch relative to their substrates tend to relieve the epitaxial strains through creation of dislocations/defects when the film thickness exceeds a critical value. The strain relaxation typically proceeds gradually over an extended range of thickness, [26] instead of an abrupt process at the critical thickness. According to the Matthews-Blakeslee model, [27] which is widely used to estimate the critical thickness at which a coherent epitaxial film begins to relax, a smaller lattice mismatch often results in a larger critical thickness. For instance, in the case of $(La_{0.7}Sr_{0.3})MnO_3$ (LSMO) films with a lattice mismatch of 0.83% grown on (001) STO substrates via PLD, it has been reported that the film remains fully strained up to 100 nm and that relaxation remains incomplete even at a thickness of 432 nm. [28] In addition to lattice mismatch, growth conditions, such as deposition rate, can also significantly influence the relaxation behavior, with high deposition rates generally delaying the onset of relaxation. [29]

Given the minimal lattice mismatch of 0.51% between bulk BNBT and the STO substrate, combined with the relatively high deposition frequency of 5 Hz employed for our Fe-doped BNBT thin films, it is reasonable to infer that the critical thickness for the onset of strain relaxation substantially exceeds 100 nm. Consequently, the Fe-BNBT layers are expected to remain fully strained well beyond this threshold, with strain relaxation remaining incomplete even at thicknesses greater than 432 nm, which is consistent with our STEM observations. In regions that are close to the substrate (< 100 nm to the substrate), the films remain fully strained with a minimal level of planar defects (see Supplementary Figure 18 (e), (f), (i), (l)). As the film thickness increases (well beyond 100 nm), partial strain relaxation occurs, accompanied by the emergence of planar defects (Supplementary Figure 18 (d), (g), (h), (k)). Upon further increase in thickness (i.e.,> ~500 nm), the BNBT films transition to a fully relaxed state. In addition to the planar defects, β-Bi_2O_3 layers are seen in Supplementary Figure 18 (j), attributed to chemical inhomogeneity. This structure evolution correlates strongly with the increasing roughness of the growing Fe-BNBT surface, compared to the atomically flat STO substrate. On

a rougher surface, the kinetic energy of incoming heavy adatoms, e.g., Bi atoms, is insufficient to support long-range surface diffusion. As a result, Bi-rich species tend to accumulate locally, leading to the segregation and formation of β-Bi_2O_3 as a secondary phase. [25]

These observations are in good agreement with the strength of the flexoelectric effect and resultant polarization of respective Fe-BNBT thin films of different thickness, i.e., the higher the density of planar density, the stronger the flexoelectric effect and overall polarization, and justify the optimal polarization in the 550 nm-thick sample. Despite the reduced density of planar density, the slight increase in polarization for the 950 nm-thick films, relative to the 750 nm-thick films, is likely attributed to the formation of super-tetragonal lattices due to the onset of the secondary phase, namely β-Bi_2O_3, which can also enhance polarization as reported before. [25]

References

1.Zeng, Z., Calle-Vallejo, F., Mogensen, M. B. & Rossmeisl, J. Generalized trends in the formation energies of perovskite oxides. *Physical Chemistry Chemical Physics* **15**, 7526-7533 (2013).
2.Becerro, A., McCammon, C., Langenhorst, F., Seifert, F. & Angel, R. Oxygen vacancy ordering in CaTiO3–CaFeO2. 5 perovskites: From isolated defects to infinite sheets. *Phase Transitions* **69**, 133-146 (1999).
3.Scott, J. & Dawber, M. Oxygen-vacancy ordering as a fatigue mechanism in perovskite ferroelectrics. *Appl. Phys. Lett.* **76**, 3801 (2000).
4.Petralanda, U., Kruse, M., Simons, H. & Olsen, T. Oxygen vacancies nucleate charged domain walls in ferroelectrics. *Phys. Rev. Lett.* **127**, 117601 (2021).
5.De Souza, R. Oxygen diffusion in SrTiO3 and related perovskite oxides. *Adv. Funct. Mater.* **25**, 6326-6342 (2015).
6.Bokov, A. A. & Ye, Z.-G. Dielectric relaxation in relaxor ferroelectrics. *Journal of Advanced dielectrics* **2**, 1241010 (2012).
7.Yan, H. *et al.* Achieved high energy density and excellent thermal stability in (1− x)(Bi0. 5Na0. 5) 0.94 Ba0. 06TiO3− x Bi (Mg0. 5Ti0. 5) O3 relaxor ferroelectric thin films. *Journal of Materials Science: Materials in Electronics* **32**, 16269-16278 (2021).
8.Hejazi, M. & Safari, A. Temperature-dependent leakage current behavior of epitaxial Bi0. 5Na0. 5TiO3-based thin films made by pulsed laser deposition. *J. Appl. Phys.* **110** (2011).
9.Sun, Y. *et al.* Large negative electrocaloric response induced by nanoscale phase transition in (Bi, Na) TiO3-based thin films. *Appl. Phys. Lett.* **122** (2023).
10.Ahmad, M., Bashir, N., Ahmad, H., Abd Jamil, A. & Suleiman, A. An overview of electrical tree growth in solid insulating material with emphasis of influencing factors, mathematical models and tree suppression. *TELKOMNIKA Indonesian Journal of Electrical Engineering* **12**, 5827-5846 (2014).
11.Wang, D. *et al.* Ferroelectric, piezoelectric, and leakage current properties of (K 0.48 Na 0.48 Li 0.04)(Nb 0.775 Ta 0.225) O 3 thin films grown by pulsed laser deposition. *Appl. Phys. Lett.* **98**, 022902 (2011).
12.Zubko, P., Jung, D. & Scott, J. Electrical characterization of PbZr 0.4 Ti 0.6 O 3 capacitors. *J. Appl. Phys.* **100**, 114113 (2006).
13.Yang, H. *et al.* Effective thickness and dielectric constant of interfacial layers of Pt⁄Bi3. 15Nd0. 85Ti3O12⁄SrRuO3 capacitors. *Appl. Phys. Lett.* **90** (2007).
14.Grove, K. M. *et al.* Impact of process conditions on chemical solution deposited BNKT thin film electromechanical properties. *SN Applied Sciences* **3**, 1-10 (2021).
15.Meng, Y., Ju, X. & Yang, X. The measurement of the dislocation density using TEM. *Mater. Charact.* **175**, 111065 (2021).
16.Ham, R. The determination of dislocation densities in thin films. *Philos. Mag.* **6**, 1183-1184 (1961).
17.Tan, Q., Li, J. & Viehland, D. Role of lower valent substituent-oxygen vacancy complexes in polarization pinning in potassium-modified lead zirconate titanate. *Appl. Phys. Lett.* **75**, 418-420 (1999).
18.Singh, S., Ishiwara, H. & Maruyama, K. Enhanced polarization and reduced leakage current in BiFeO3 thin films fabricated by chemical solution deposition. *J. Appl. Phys.* **100** (2006).
19.Bendahhou, A., Chourti, K., Loutou, M., El Barkany, S. & Abou-Salama, M. Impact of rare earth (RE 3+= La 3+, Sm 3+) substitution in the A site perovskite on the structural, and electrical properties of Ba (Zr 0.9 Ti 0.1) O 3 ceramics. *RSC Adv.* **12**, 10895-10910 (2022).

20.Lin, Q. *et al.* Large Piezoelectricity and Ferroelectricity in Mn-Doped (Bi0. 5Na0. 5) TiO3-BaTiO3 thin film prepared by pulsed laser deposition. *J. Am. Ceram. Soc.* **99**, 2347-2353 (2016).
21.Sun, Y., Yang, J., Li, S. & Wang, D. Defect engineering in perovskite oxide thin films. *Chem. Commun.* **57**, 8402-8420 (2021).
22.Shuai, Y. *et al.* Decisive role of oxygen vacancy in ferroelectric versus ferromagnetic Mn-doped BaTiO3 thin films. *J. Appl. Phys.* **109** (2011).
23.Maier, R., Pomorski, T., Lenahan, P. & Randall, C. Acceptor-oxygen vacancy defect dipoles and fully coordinated defect centers in a ferroelectric perovskite lattice: Electron paramagnetic resonance analysis of Mn2+ in single crystal BaTiO3. *J. Appl. Phys.* **118** (2015).
24.Chang, H. *et al.* Effects of oxygen mobility in La–Fe-based perovskites on the catalytic activity and selectivity of methane oxidation. *ACS Catalysis* **10**, 3707-3719 (2020).
25.Sun, Y. *et al.* Ultrahigh energy storage density in glassy ferroelectric thin films under low electric field. *Adv. Sci.* **9**, 2203926 (2022).
26.Meyer, T. L., Jiang, L., Park, S., Egami, T. & Lee, H. N. Strain-relaxation and critical thickness of epitaxial La1. 85Sr0. 15CuO4 films. *APL Mater.* **3** (2015).
27.Matthews, J. W. & Blakeslee, A. E. Defects in epitaxial multilayers: I. Misfit dislocations. *J. Cryst. Growth* **27**, 118-125 (1974).
28.Maurice, J.-L. *et al.* Strain relaxation in the epitaxy of La2/3Sr1/3MnO3 grown by pulsed-laser deposition on SrTiO3 (001). *Philos. Mag.* **83**, 3201-3224 (2003).
29.Kawai, M. *et al.* Deposition Rate Effect on Critical Thickness of BaTiO3 Epitaxial Thin Film Grown on SrTiO3 (001). *MRS Online Proceedings Library (OPL)* **1034**, 1034-K1010-1004 (2007).